Chinese Physics Letters **41**, 044205 (2024)

Reversible Optical Isolators and Quasi-Circulators Using a Magneto-Optical Fabry–Pérot Cavity

Tiantian Zhang(张天天)[1], Wenpeng Zhou(周文鹏)[1], Zhixiang Li(李志向)[1], Yutao Tang(唐宇涛)[2],
Fan Xu(许帆)[2], Haodong Wu(吴浩东)[1], Han Zhang(张涵)[3], Jiang-Shan Tang(唐江山)[1*],
Ya-Ping Ruan(阮亚平)[1*], and Keyu Xia(夏可宇)[1,4*]

[1]*College of Engineering and Applied Sciences, National Laboratory of Solid State Microstructures, and Collaborative Innovation Center of Advanced Microstructures, Nanjing University, Nanjing 210093, China*
[2]*Shenzhen Shaanxi Coal Hi-tech Research Institute Co., Ltd, Shenzhen 518083, China*
[3]*School of Physics, Nanjing University, Nanjing 210023, China*
[4]*Jiangsu Key Laboratory of Artificial Functional Materials, Nanjing University, Nanjing 210023, China*

(Received 29 January 2024; accepted manuscript online 3 April 2024)

Nonreciprocal optical devices are essential for laser protection, modern optical communication and quantum information processing by enforcing one-way light propagation. The conventional Faraday magneto-optical nonreciprocal devices rely on a strong magnetic field, which is provided by a permanent magnet. As a result, the isolation direction of such devices is fixed and severely restricts their applications in quantum networks. In this work, we experimentally demonstrate the simultaneous one-way transmission and unidirectional reflection by using a magneto-optical Fabry–Pérot cavity and a magnetic field strength of 50 mT. An optical isolator and a three-port quasi-circulator are realized based on this nonreciprocal cavity system. The isolator achieves an isolation ratio of up to 22 dB and an averaged insertion loss down to 0.97 dB. The quasi-circulator is realized with a fidelity exceeding 99% and an overall survival probability of 89.9%, corresponding to an insertion loss of ∼ 0.46 dB. The magnetic field is provided by an electromagnetic coil, thereby allowing for reversing the light circulating path. The reversible quasi-circulator paves the way for building reconfigurable quantum networks.

DOI: 10.1088/0256-307X/41/4/044205

Nonreciprocal optical devices (NRODs), including optical isolators and circulators, are critical components in the classical optics regime and photonic quantum systems,[1–3] as they protect lasers and sensitive signals by isolating or separating the backscattered light.[4] In the quantum domain, circulators play a crucial role in the field of quantum information and are essential in quantum network architectures.[5,6]

The optical nonreciprocity that breaks the time-reversal symmetry of light propagation is usually attained by polarizers and Faraday rotators, which rely on magnetically biased materials.[7–10] However, limited by the weak magneto-optical (MO) effect, such conventional NRODs typically require strong magnetic fields,[11–14] which are generated by permanent magnets, hindering the reconfigurability of NRODs in practical optical applications. Dynamically reversing the propagation direction of light in NRODs is highly desirable, particularly for reconfigurable quantum networks.[2,15–25]

To circumvent the severe constraints imposed by strong magnetic fields, one effort is devoted to magnet-free optical nonreciprocity, including chiral quantum optics systems,[5,19,26–31] spatiotemporal modulation of the medium,[32–34] optical nonlinearity,[3,35–42] the Doppler effect,[20,43–47] optomechanical resonators,[48–52] spinning resonators,[53] etc. An alternative avenue involves enhancing the MO effect by exploiting strong MO materials,[54–57] and cavity-enhanced strategies.[21,58–61] Moreover, unidirectional invisibility also attracts intensive attention, engineering light reflection in unprecedented manners across diverse systems and structures.[62–66] The simultaneous one-way transmission and unidirectional reflection is fundamentally interesting, but its realization remains a challenge.

Thanks to the fact that light repeatedly passes through the object in an optical resonant system, the interaction between light and matter can be greatly enhanced in a Fabry–Pérot (F-P) cavity.[67] The use of F-P cavities to amplify Faraday rotation for achieving isolator effects has been extensively studied in theory,[68–71] but it has rarely been experimentally verified. This configuration is known as an MO F-P (MOFP) cavity[68] or a resonant optical Faraday rotator.[70] Furthermore, the implementation of more feature-rich reversible optical circulators or quasi-circulators using this system is still elusive.

In this Letter, we demonstrate reversible optical isolators and three-port quasi-circulators based on the MOFP cavity. In comparison to conventional MO nonreciprocal devices, our scheme requires a smaller magnetic field. Notably, this approach enables electrically controlling the magnetic direction, thereby enabling reversible optical isolators and quasi-circulators. Moreover, we achieve the simultaneous one-way transmission and unidirectional reflection. The reported reversible NRODs may pave the

---

*Corresponding authors. Email: js.tang@nju.edu.cn; ruanyaping@nju.edu.cn; keyu.xia@nju.edu.cn

way for reconfigurable quantum networks.[2,15–25]

System and Model. Our reversible optical isolator and quasi-circulator consist of an MOFP cavity and two sets of polarization beam splitters (PBSs) and quarter wave plates (QWPs). Their schematic diagrams for opposite isolation directions are shown in Figs. 1(a) and 1(b). The MOFP cavity is composed of an F-P cavity and a piece of terbium gallium garnet (TGG) crystal, a type of MO crystal. The F-P cavity supports two degenerate circularly polarized optical modes, σ^+ and σ^-, with the same frequency ω_0. Here, to avoid confusion, σ^+- and σ^--polarized fields are defined by the rotating direction of the electric-field vectors with respect to the magnetic field direction.[31,72] This is different from the optical case, where polarization is defined as either left-handed or right-handed circular polarization by observing the rotation of the electric field vector in relation to the direction of light propagation.[73] Therefore, the σ^+ and σ^- polarizations can be either left-handed or right-handed circular polarization as defined in optics. This is essentially because the refractive index response of an MO crystal to optical polarizations depends on the rotation of the electric-field vectors relative to its quantization axis (z-axis), which corresponds to the direction of the magnetic field in our system. In the case of σ^+- and σ^--polarized fields, the refractive indices of the MO crystal are denoted as n_+ and n_-, respectively. This leads to the breaking of the originally degenerate resonant frequencies ω_0 into ω_+ and ω_-.

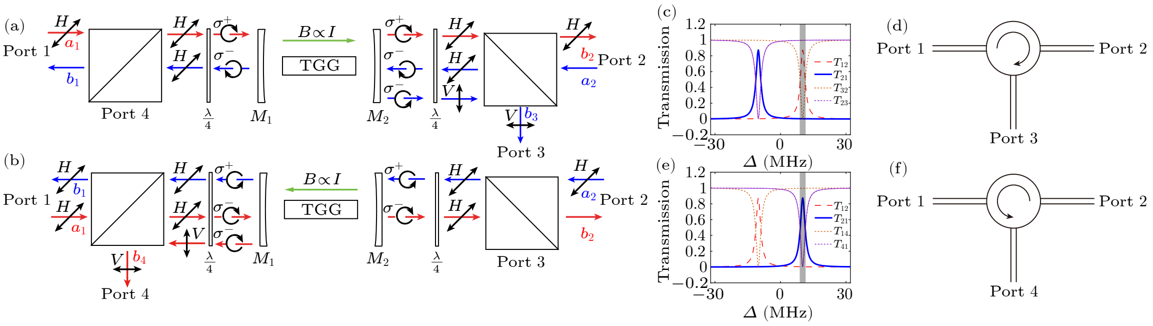

Fig. 1. [(a), (b)] Conceptual schematics of the reversible optical isolators and quasi-circulators. Experimental diagrams of the clockwise (CW) (a) and counterclockwise (CCW) (b) configurations comprise a magneto-optical Fabry–Pérot (MOFP) cavity, a pair of quarter wave plates (QWPs), and a pair of polarization beam splitters (PBSs), respectively. The magnetic direction of the CCW configuration is opposite to that of the CW configuration. The combination of PBSs and QWPs locks the $\sigma^\pm$ polarization and the optical propagation direction in the MOFP cavity. Black arrows indicate local optical polarization. Here, σ^+ and σ^- polarizations are defined by the rotating direction of the electric-field vectors relative to the direction of the magnetic field. The circulation of the polarized light is achieved through PBSs. TGG: terbium gallium garnet. [(c), (e)] Schematic transmission spectra of the CW (c) and CCW (e) quasi-circulators versus the detuning $\Delta = \omega - \omega_0$, respectively. The shaded areas indicate the operating band of the isolator and quasi-circulator. [(d), (f)] Schematic CW (d) and CCW (f) quasi-circulators depicting the flowing direction of light in the CW and CCW configurations, respectively.

By utilizing two sets of the PBSs and QWPs, the locking of $\sigma^\pm$ polarization and the optical propagation direction can be realized in the MOFP cavity,[31,72] as shown by the black arrows in Figs. 1(a) and 1(b). In this system, the input field aligned with the magnetic direction exhibits σ^+ polarization, whereas its antiparallel counterpart manifests as σ^- polarization. This results in a chiral refractive index response within the MOFP cavity. In this case, the time-reversal symmetry of the system is broken, leading to nonreciprocal resonant transmission spectra. However, in the absence of MO crystals, the system becomes reciprocal.

Next, we investigate the transmission properties of the system, which can be expressed as[67,74–76]

$$T_\pm = \frac{\kappa_{\rm ex}^2}{\delta_\pm^2 + \kappa_\pm^2/4}, \quad R_\pm = \frac{\delta_\pm^2 + \kappa_i^2/4}{\delta_\pm^2 + \kappa_\pm^2/4}, \qquad (1)$$

where T_+ (T_-) and R_+ (R_-) denote the transmittance and reflectance of the $\sigma^+(\sigma^-)$ incident light, respectively. The losses $\kappa_\pm = \kappa_{\rm ex,\,1} + \kappa_{\rm ex,\,2} + \kappa_i + \kappa_{i,\,\pm}$ correspond to the total decay rates of σ^+- and σ^--polarized fields in the MOFP cavity. Here, $\kappa_{\rm ex,\,1}$ and $\kappa_{\rm ex,\,2}$ describe the extrinsic losses from the cavity mirrors, κ_i represents the intrinsic loss of the bare cavity, and $\kappa_{i,\,+}$ ($\kappa_{i,\,-}$) arises from the absorption of σ^+- (σ^--) polarized field by the MO crystal. We set $\kappa_{\rm ex,\,1} = \kappa_{\rm ex,\,2} = \kappa_{\rm ex}$ in the theoretical model. The detunings is $\delta_+ = \omega - \omega_+$ ($\delta_- = \omega - \omega_-$), where ω is the frequency of the input light. It is obvious that the system exhibits different transmission and reflection characteristics when different polarized light incidences occur. By the merit of this property, optical nonreciprocity can be realized.

Since the σ^+- and σ^-- polarizations are defined with respect to the magnetic field's direction, altering the orientation of the magnetic field allows for control over the polarization of incident fields, as illustrated in Figs. 1(a) and 1(b). In the case of traditional Faraday MO devices, the requirement for strong magnetic fields presents a challenge when attempting to change the magnetic field's direction. However, in our system, only a relatively weak magnetic field is necessary, thus eliminating this issue, which will be thoroughly explained. Hence, our device exhibits reconfigurability through manipulation of the magnetic field orientation.

We utilize the transfer matrix method to investigate the transmission properties of the system.[77] The notations for field components $\{\boldsymbol{a}\}$ and $\{\boldsymbol{b}\}$ are shown in Fig. 1. We first study the situation in Fig. 1(a). The transmission relation between the incident light vector $\boldsymbol{a}$ ($\boldsymbol{a} = \{a_1, a_2, a_3, a_4\}^{\mathrm{T}}$) and the outgoing light vector $\boldsymbol{b}$ ($\boldsymbol{b} = \{b_1, b_2, b_3, b_4\}^{\mathrm{T}}$) can be written as

$$\begin{pmatrix} b_2 \\ b_3 \end{pmatrix} = \begin{pmatrix} T_+ & 0 & R_+ \\ 0 & R_- & 0 \end{pmatrix} \begin{pmatrix} a_1 \\ a_2 \\ a_3 \end{pmatrix}, \tag{2}$$

where the subscript represents the incident and outgoing light of port i. Figure 1(c) shows the theoretical transmission spectra from ports 1 and 2, respectively. Consider the input within the shaded frequency range in Fig. 1(c). When incident light enters through port 1, it excites the σ^+- polarized mode. At the resonance, that is, when $\delta_+ = 0$, in the case of $\kappa_{\mathrm{ex}} \gg \kappa_i + \kappa_{i,\pm}$, $T_+ \simeq 1$ and $R_+ \simeq 0$ (see the dashed red curve), indicating that the forward light is nearly fully transmitted with minimal reflection. However, when incident light enters through port 2, it corresponds to the excitation of the σ^-- polarized field, resulting in $\delta_- \gg \kappa_-$ due to the different resonant frequencies. This leads to $T_- \simeq 0$ and $R_- \simeq 1$ (see the solid blue curve), signifying that the backward input light is nearly completely reflected and transmits to port 3. Hence, the exotic propagation characteristics of forward and backward light exhibit nonreciprocal transmission and unidirectional invisibility.[62] By leading the reflected light to a port other than the input one, we can construct a quasi-circulator. The optical path implements a clockwise (CW) three-port quasi-circulator, along port 1 → 2 → 3,[3] as shown in Figs. 1(a) and 1(d). Synthesizing the above content, the ideal transmission matrix of the CW quasi-circulator can be derived as

$$T_{\mathrm{id,CW}} = \begin{pmatrix} 1 & 0 & 0 \\ 0 & 1 & 0 \end{pmatrix}. \tag{3}$$

When the magnetic field is reversed, light propagates along opposite direction, corresponding to the situation in Fig. 1(b). Similarly, the transfer matrix can be written as

$$\begin{pmatrix} b_1 \\ b_4 \end{pmatrix} = \begin{pmatrix} 0 & T_+ & R_+ \\ R_- & 0 & 0 \end{pmatrix} \begin{pmatrix} a_1 \\ a_2 \\ a_4 \end{pmatrix}. \tag{4}$$

The reversal of the magnetic field causes the circularly polarized fields excited by different ports to also reverse. Consequently, the light path exhibits a counterclockwise (CCW) circulation of photons (port 2 → 1 → 4), see Figs. 1(e) and 1(f). Based on this, we obtain the ideal transmission matrix of the CCW quasi-circulator,

$$T_{\mathrm{id,CCW}} = \begin{pmatrix} 0 & 0 & 1 \\ 1 & 0 & 0 \end{pmatrix}. \tag{5}$$

In the following, we refer to Figs. 1(a) and 1(b) as CW and CCW configurations, respectively.

In this study, we designate our three-port circulator as a "quasi-circulator". In practical applications, this three-port quasi-circulator can fulfill the majority of requirements for light circulation.[3] Furthermore, the system discussed above has the potential to function as a four-port close-loop circulator, with the 4×4 transmission matrices. To illustrate the potential for upgrading to a four-port circulator, we provide a detailed schematic diagram and accompanying discussions in the Supplementary Materials.

We consider an MOFP cavity with an effective optical path L. When a magnetic field B is applied to the MO crystal with length l and the Verdet constant V, the optical rotation angle ϕ and the resulting shift are[78]

$$\phi = VBl, \quad \omega_+ - \omega_- = \frac{2\mathrm{FSR} \times \phi}{\pi}, \tag{6}$$

where FSR is the free spectral range (FSR) of the MOFP cavity. $\mathrm{FSR} = c/2L$, with c being the speed of light in vacuum, $c = 3 \times 10^8$ m/s. Thus, the impact of the magnetic field on the frequency shift can be expressed as

$$\omega_+ - \omega_- = \frac{2\mathrm{FSR} \times V \times l \times B}{\pi}. \tag{7}$$

This equation shows that the relationship between frequency shift and magnetic field strength is linear.

Finally, we investigate the impact of magnetic field strength on the isolation ratio ($\mathcal{I}$). Based on Eqs. 2 and 4, we can derive an expression for the effect of magnetic field strength on the isolation ratio. Taking the CW quasi-circulator as an example and the approximation $\kappa_{\mathrm{ex}} \gg \kappa_i$, the isolation ratio of ports 1 and 2 is defined as

$$\begin{aligned} \mathcal{I} &= 10\log_{10}\Big(\frac{T_{12}}{T_{21}}\Big) = 10\log_{10}\Big(\frac{T_+ a_1 + R_+ a_3}{T_- a_2}\Big) \\ &\simeq 10\log_{10}\Big[\frac{4(\omega_+ - \omega_-)^2 + \kappa_-^2}{\kappa_+^2}\Big]. \end{aligned} \tag{8}$$

Here, we have assumed that $a_1 = a_2 = a_3$ to simplify the calculation. By substituting Eq. 7 into Eq. 8, we further have

$$\mathcal{I} = 10\log_{10}\Big[\frac{16(\mathrm{FSR} \times V \times l \times B)^2 + \pi^2\kappa_-^2}{\pi^2\kappa_+^2}\Big]. \tag{9}$$

Equation (9) reveals that the isolation ratio is expected to increase as the magnetic field strength increases. This also explains why traditional Faraday MO devices require strong magnetic fields. However, in the MOFP cavity system, the existence of the cavity (allowing FSR to be regulated) provides the possibility of achieving high isolation ratio with a small magnetic field. The insertion loss (IL) of the isolator is defined as[3,43]

$$\mathrm{IL} = -10\log_{10}(T_f), \tag{10}$$

where T_f represents the transparent direction. It is T_{12} in Fig. 1(a) or T_{21} in Fig. 1(b).

The performance of a quasi-circulator can be quantified with the average photon survival probability η and the fidelity $\mathcal{F}$. The survival probability of the probe light is given by $\eta_i = \sum_k T_{ik}$, and T_{ik} represents the transmission rate of light from port i to port k. The average photon survival probability for quasi-circulator is $\eta = \sum_i \eta_i/2$.[3,43] The corresponding insertion loss of the quasi-circulator is $\mathrm{IL} = -10\log_{10}(\eta)$. The fidelity $\mathcal{F}$ is evaluated by examining the overlap between the renormalized transmission matrix $\tilde{T} = (T_{ij}/\eta_i)$ and the ideal one T_{id}. The average operation fidelity of the quasi-circulator can be calculated as[5,43]

$$\mathcal{F} = \frac{\mathrm{Tr}[\tilde{T}T_{\mathrm{id}}^{\mathrm{T}}]}{\mathrm{Tr}[T_{\mathrm{id}}T_{\mathrm{id}}^{\mathrm{T}}]}. \tag{11}$$

It is important to note that in this framework, η and $\mathcal{F}$ are not limited to describing quantum systems, and their purpose is strictly characterize the performance of the quasi-circulator. The significance of these symbols lies in the ability to quantify the level of agreement between the actual scattering matrix and the ideal scattering matrix of the quasi-circulator. We leverage the robust mathematical frameworks and analytical methodologies established within the field of quantum optics to better characterize our devices.

Experimental Setup. The schematic experimental setup is illustrated in Fig. 2. We experimentally implement the proposed scheme based on an MOFP cavity system embedded with a TGG crystal. The crystal is $l = 18\,\mathrm{mm}$ in length and coated with a broadband transmission-enhancing film on both facets. The coated film covers the entire operating frequency band. The TGG crystal has an extremely high transmittance, $V = 78.5\,\mathrm{rad{\cdot}T^{-1}{\cdot}m^{-1}}$ and the refractive index $n_0 = 1.95$ in the absence of the magnetic field. The MOFP cavity is constructed by using two high-reflection concave mirrors ($r = 99\%$ reflectivity), denoted as M_1 and M_2. Each mirror has a curvature radius of 100 mm. The spatial distance between the two mirrors is about 182 mm, yielding an effective optical length $L = 200\,\mathrm{mm}$ for the whole MOFP cavity. We obtain $\gamma = n_0 l/L = 0.18$, representing the ratio between the effective optical paths of the crystal and the cavity. The MOFP cavity is positioned between two sets of QWPs and PBSs, collectively forming the optical momentum-spin locking apparatus.[31] The frequency difference $\omega_+ - \omega_-$ increases with the ratio γ.[79]

The fast axis of each QWP is oriented at an angle of 45° relative to the horizontal direction, and the fast axes of the two QWPs are configured mutually orthogonally. Upon passing through the optical momentum-spin locking apparatus, all incident light undergoes spin modulation, resulting in distinct optical polarization states. Specifically, the light propagating within the MOFP cavity in the direction of the magnetic field is modulated into σ^+ polarized light, whereas the light traveling in the opposite direction is modulated into σ^- polarized light. In addition, we insert a pair of BSs into the optical path so that the signal can be emitted from ports 1 and 2. A pair of PBSs enable the emission of signals with different polarizations from ports 3 and 4. In this way, the output beam of quasi-circulator can be monitored by the PD 1, PD 2, PD 3, and PD 4, which correspond to ports 1, 2, 3, and 4, respectively. The experiment operates at temperature of 25 ℃.

The laser beams used in the experiment are derived from a tunable external cavity semiconductor laser operating at a wavelength of 795 nm and have a waist diameter of 159 µm. These laser beams are directed towards the optical quasi-circulators via a fiber splitter that bifurcates the signal into two separate paths. Subsequently, they enter the optical quasi-circulator at ports 1 and port 2, respectively.

An electromagnetic coil is used to generate a relatively weak magnetic field for the MO crystal, as shown in Fig. 2. The relationship between the strengths of the magnetic field (B) and the currents (I) is $B = \beta I$ with the generating efficiency $\beta \approx 25\,\mathrm{mT/A}$. It is worth noting that the magnetic field generated by the energized coil is significantly greater than that of the Earth, thus making any potential impact from the latter negligible. Therefore, we can reverse the direction of the magnetic field by changing the direction of the current. This feature allows for the straightforward reversal of the optical isolators and quasi-circulators implemented within the system.

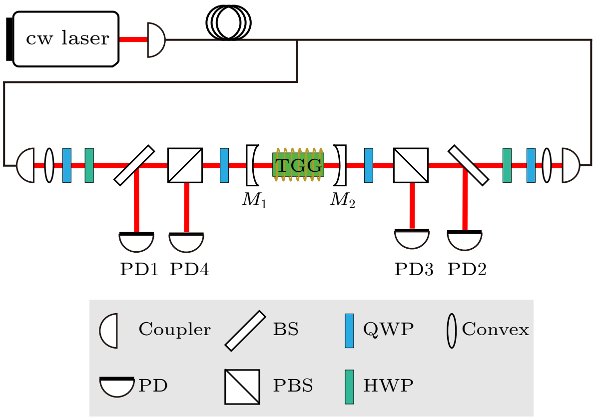

Fig. 2. Schematic experimental setup for the optical isolators and quasi-circulators based on the MOFP cavity. PD: photon detector; BS: beam splitter; PBS: polarization beam splitter; M: mirror; QWP: quarter-wave plate; HWP: half-wave plate; Convex: convex lens.

Results. To investigate the reversible optical nonreciprocal behavior, we measured the transmission of the beams in the system for both left-to-right (corresponding to CW configuration) and right-to-left (corresponding to CCW configuration) magnetic directions, as shown in Figs. 3 and 5, respectively. Swiftly switching between the two configurations can be achieved by changing the direction of the current. During our measurement, the 795 nm laser beams are incident simultaneously on both ports 1 and 2.

Initially, we characterize the optical nonreciprocity of the CW configuration. As demonstrated above, the magnetic field significantly enhances the circular dichroism of TGG crystal. The transmission spectra measured at each port of the CW configuration are shown in Fig. 3(a) for the analysis of multiple peaks and in Fig. 3(b) for the analysis of the individual peaks.

It can be observed that the resonant frequency shifts as expected, thereby introducing nonreciprocal transmission within a specific frequency range (indicated by the shaded areas). When the incident light frequency matches the resonance frequency of the CW configuration, the transmission from port 1 to port 2 is $T_{12}(\omega_+) \approx 80\%$, corresponding to an insertion loss of 0.97 dB, while the opposite transmission $T_{21}(\omega_-) \approx 0.45\%$. Thus, in CW configuration, a high-performance optical isolator can be implemented with ports 1 and 2. The isolation ratio and insertion loss are shown in Figs. 3(c) and 3(d), respectively. The isolation ratio of incident beam at the resonance frequency (ω_+) reaches a maximum of 22.4 dB. The resonance frequency splits by $|\omega_+ - \omega_-| \approx 47.2$ MHz.

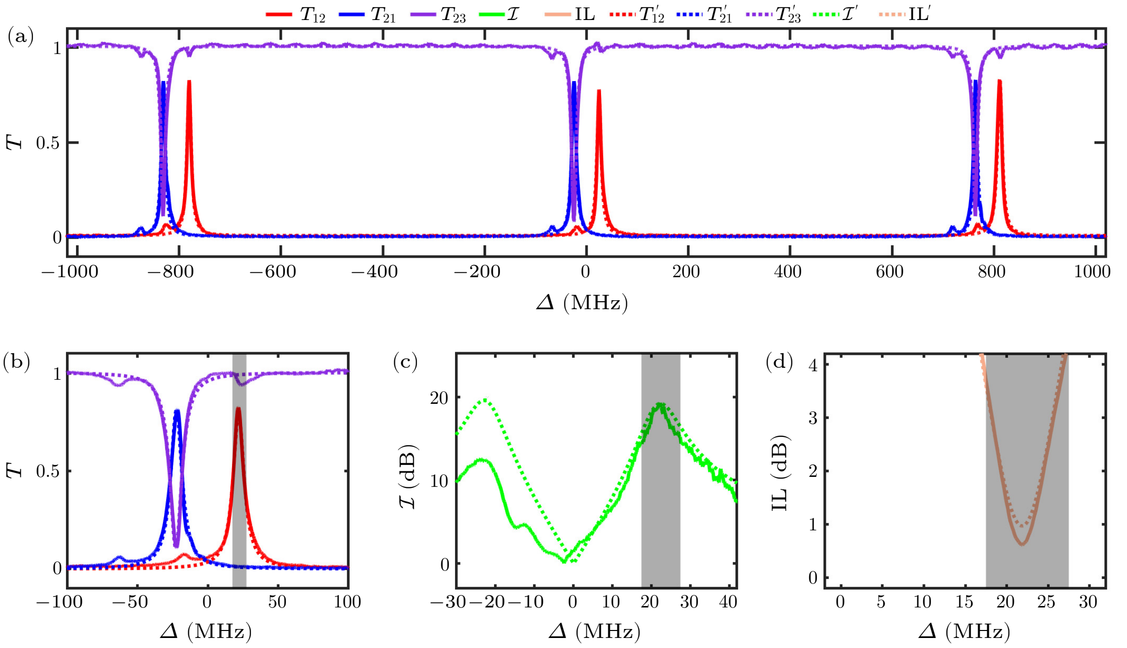

Fig. 3. Performance of optical isolators based on CW configuration. [(a), (b)] The overall (a) and detailed (b) measured transmission spectra between different ports. The solid curves correspond to the experimentally measured values, denoted as T'_{nm}. The dotted curves correspond to the theoretically calculated values, denoted as T_{nm}. In this context, T_{nm} signifies the transmission coefficient form port m to port n, where m, $n \in \{1, 2, 3, 4\}$. Fitting parameters: $\kappa_{\rm ex} = 4.3$ MHz, $\kappa_i = 0.7$ MHz, $\kappa_{i,+} = 0.16$ MHz, $\kappa_{i,-} = 0.4$ MHz, $B = 50$ mT. [(c), (d)] Isolation ratio (c) and insertion loss (d) of ports 1 and 2 as a function of the detuning Δ, respectively. The shaded regions indicate effective operating frequency range of the CW configuration.

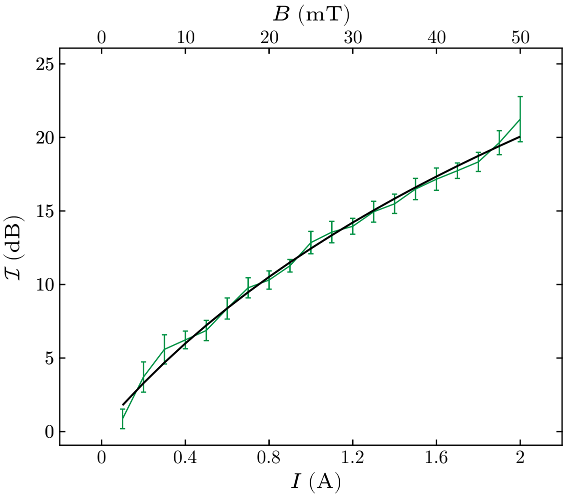

Fig. 4. Isolation ratio in CW configuration versus the current strength and the magnetic field strength. The green curve is calculated from the experimental data; the black curve is the theoretical results. Other parameters are as those in Fig. 3.

Figure 4 shows the isolation ratio versus the current strength. The green curve represents the experimental results for the isolation ratio, while the black curve is for the theoretical result obtained by substituting experimental parameters into Eq. (9). When the current amplitude increases from 0 A to 2 A, the effective magnetic field strengths applied to the TGG crystal varies from 0 mT to 50 mT. This magnetic field is considerably less than that required for the conventional MO isolator. The latter typically operates at the order of several Tesla magnitudes.[80–83] The isolation ratio increases as the magnetic field strength increases, with a maximum value greater than 20 dB, implying that we can indeed control the isolation ratio of the isolator by adjusting the current intensity. In fact, the value of β can be increased by the coil turn number, leading to a significant decrease in the required current.

For comparison with the CW configuration, performance of the optical isolator in the CCW configuration is also shown in Fig. 5. The magnetic field can be reversed by changing the direction of the current. In this case, when the incident light frequency matches the resonance frequency of the CCW configuration without the need to adjust any other parameters of the system, see Figs. 5(a) and 5(b). The transmission from port 2 to port 1 is $T_{21}(\omega_+) \approx 80.9\%$. It is much larger than the opposite transmission $T_{12}(\omega_-) \approx 0.6\%$. The corresponding insertion loss is IL $= 0.92$ dB. The frequency difference between the two resonance modes is $|\omega_+ - \omega_-| \approx 47.1$ MHz. The isolation ratio and insertion loss of the CCW quasi-circulator are illustrated in Figs. 5(c) and 5(d), respectively. At the resonant frequency, the incident beam can achieve a maximum isolation ratio as high as 22.1 dB. The bandwidth is about 10 MHz for $\mathcal{I} > 11$ dB. Furthermore, all the theoretical results in Figs. 3–5 precisely match the corresponding experimental data. The CCW quasi-circulator shows the similar dependence of the isolation ratio on the current strength (not shown here).

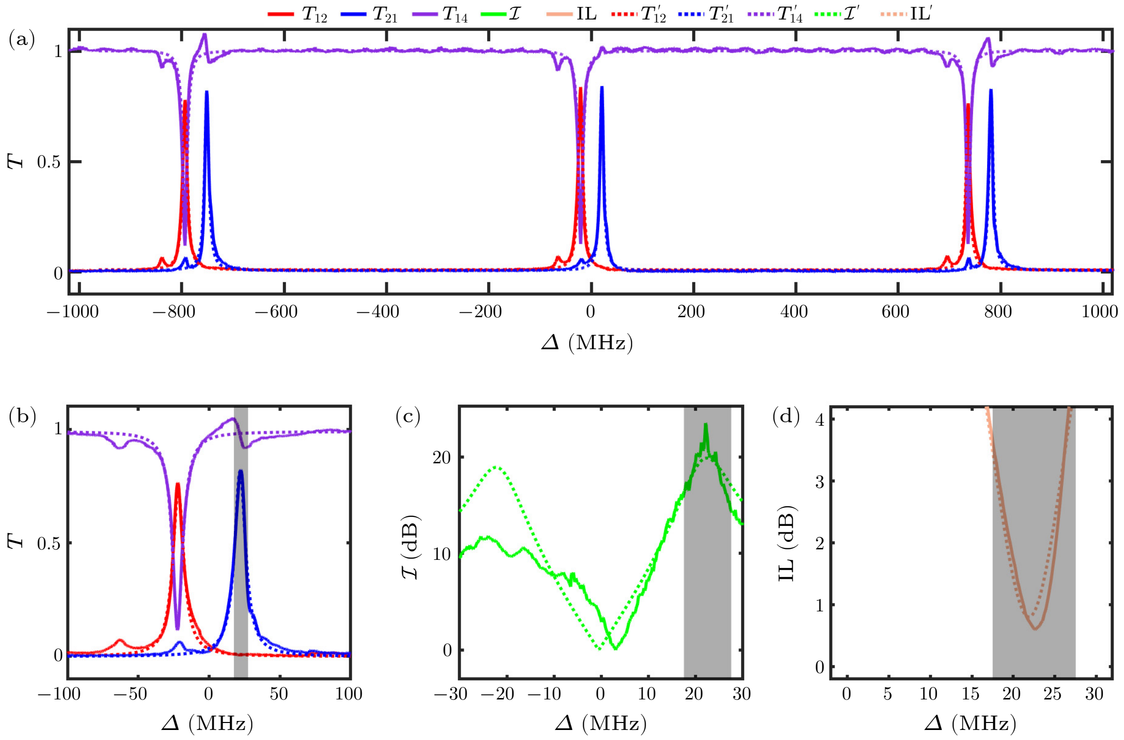

Fig. 5. Performance of optical isolators based on CCW configuration. [(a), (b)] The overall (a) and detailed (b) measured transmission spectra between ports. The solid curves represent the experimentally measured values, labeled as T'_{nm}, while the dotted curves depict the theoretically calculated values with the same parameters as in Fig. 3, denoted as T_{nm}. The fitting parameters are $\kappa_{\text{ex}} = 4.3$ MHz, $\kappa_i = 0.6$ MHz, $\kappa_{i,+} = 0.1$ MHz, $\kappa_{i,-} = 0.4$ MHz. [(c), (d)] Isolation ratio (c) and insertion loss (d) of ports 1 and 2 as a function of the detuning Δ, respectively. Similarly, the shaded regions indicate effective operating frequency range of the CCW configuration.

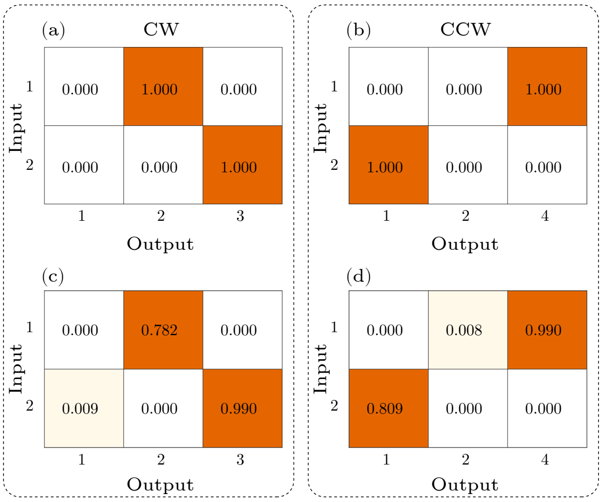

(a) CW

Input \ Output	1	2	3
1	0.000	1.000	0.000
2	0.000	0.000	1.000

(b) CCW

Input \ Output	1	2	4
1	0.000	0.000	1.000
2	1.000	0.000	0.000

(c)

Input \ Output	1	2	3
1	0.000	0.782	0.000
2	0.009	0.000	0.990

(d)

Input \ Output	1	2	4
1	0.000	0.008	0.990
2	0.809	0.000	0.000

Fig. 6. Transmission matrices of optical quasi-circulators. [(a), (c)] Ideal (a) and measured (c) transmission matrices of the CW quasi-circulator. [(b), (d)] Ideal (b) and measured (d) transmission matrices of the CCW quasi-circulator. Numbers inside the color squares represent the transmission between the two ports. Zero transmissions are indicated in the white regions. Other parameters are the same as those in Fig. 3.

It is worth noting that we also observe unidirectional reflection in both the CW and CCW configurations. The reflected light can lead to a third port to form a quasi-circulator. Now we evaluate the performance of the three-port quasi-circulators. In the CW configuration in Fig. 1(c), the transmission T_{23} from port 2 to port 3 can reach about 99% within the nonreciprocal region, see the purple curve in Fig. 3(b). Therefore, the system exhibits the function of an optical quasi-circulator with light flowing along port $1 \to 2 \to 3$. The ideal and measured transmission matrices of the CW quasi-circulator are displayed in Figs. 6(a) and 6(c). The fidelity reaches $\mathcal{F} \approx 99.5\%$ and the average photon survival probability is $\eta = 89.4 \pm 0.4\%$.

Similarly, by reversing the magnetic field, a CCW photonic quasi-cyclic direction from port 2 to port 1 and then to port 4 (port $2 \to 1 \to 4$) can be established using the CCW configuration. We refer to this as a CCW three-port quasi-circulator. Ideal and measured transmission matrix are shown in Figs. 6(b) and 6(d). In the CCW three-port quasi-circulator, we can achieve a fidelity of $\mathcal{F} \approx 99.6\%$ and an average photon survival probability of $\eta = 90.4 \pm 0.1\%$. The averaged survival probability of two cases is 89.9%, yielding an insertion loss of ~ 0.46 dB.

It is worth mentioning that although we typically manually change the direction of the magnetic field when measuring spectral line data, experimental results show that the system can switch between the CW and CCW configurations in just 1 μs, as shown in Fig. 7. Furthermore, through more sophisticated circuit design, this switching time can be further reduced, providing a very promising prospect for practical applications of our system.

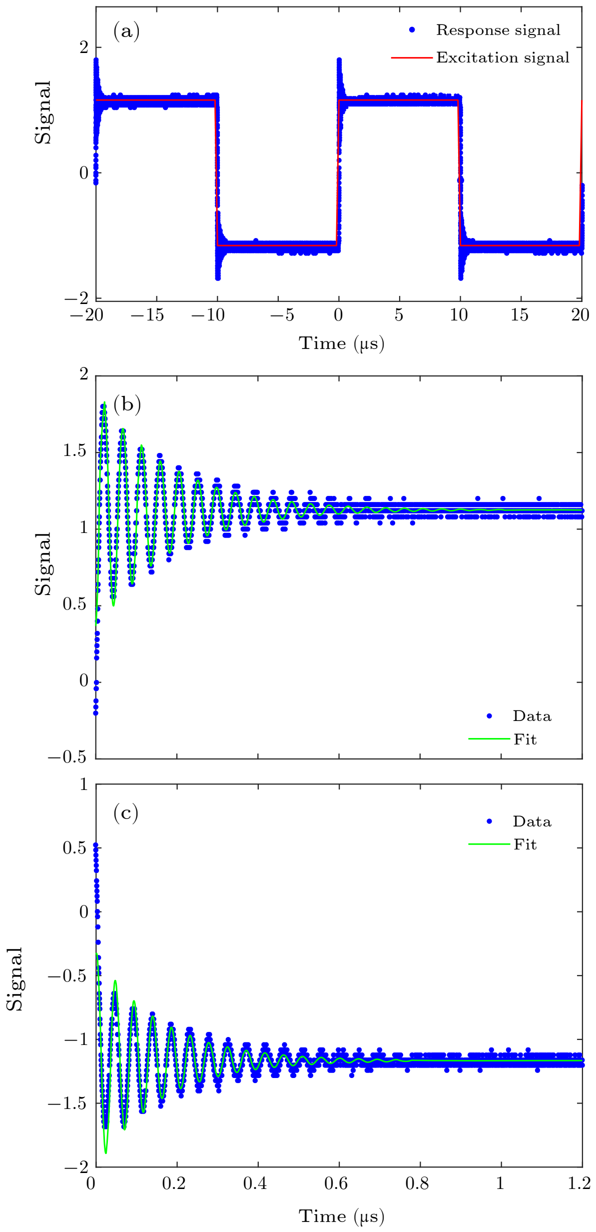

Fig. 7. Performance of the system switching. (a) Overall performance of the system signals. The red line represents the waveform of the excitation signal generated by the power supply, while the blue dots represent the waveform of the response signal detected by the oscilloscope. [(b), (c)] The waveform of the rising edge (b) and falling edge (c) of the actual detected response signal, where the blue dots represent the actual detected waveform, and the green curve represents the theoretically fitted waveform.

In summary, we have demonstrated the reversible isolators and three-port optical quasi-circulators via combination of the MOFP cavity and special polarization modulation. The optical isolator achieves an isolation ratio of 22 dB and a low insertion loss of 0.97 dB under a 50 mT magnetic field. This magnetic field is significantly lower than that required in commercial MO nonreciprocal devices and is provided by an electromagnetic coil.[13,80–83] The fidelity of the three-port quasi-circulator exceeds 99% while maintaining an overall averaged survival probability close to 89.9%, corresponding to a loss of about 0.46 dB. Such a low-loss reversible quasi-circulator is vital for reconfigurable quantum networks.

The magnetic field needed for our devices can be decreased further by employing MO materials with higher Verdet constants, such as yttrium iron garnet (YIG), $V > 10^3\,\mathrm{rad{\cdot}T^{-1}{\cdot}m^{-1}}$.[84,85] On the other hand, larger spectral splitting can be obtained by increasing the ratio γ.[79] When γ increases to 0.9, only a 2 mT magnetic field is needed for the our quasi-circulators if using the YIG crystal. Furthermore, in the case of employing magnetic-optical materials with $V > 10^5\,\mathrm{rad{\cdot}T^{-1}{\cdot}m^{-1}}$,[55,61] the magnetic field required for our device would be weaker than 1 Gauss.

Acknowledgements. This work was supported by the National Key R&D Program of China (Grant No. 2019YFA0308700), the National Natural Science Foundation of China (Grant Nos. 11890704, 92365107, and 12305020), the Program for Innovative Talents and Teams in Jiangsu (Grant No. JSSCTD202138), the Shccig-Qinling Program, the China Postdoctoral Science Foundation (Grant No. 2023M731613), and the Jiangsu Funding Program for Excellent Postdoctoral Talent (Grant No. 2023ZB708).

References

[1] Sathyamoorthy S R, Tornberg L, Kockum A F, Baragiola B Q, Combes J, Wilson C M, Stace T M, and Johansson G 2014 *Phys. Rev. Lett.* **112** 093601

[2] Daiss S, Langenfeld S, Welte S, Distante E, Thomas P, Hartung L, Morin O, and Rempe G 2021 *Science* **371** 614

[3] Tang L, Tang J, Chen M, Nori F, Xiao M, and Xia K 2022 *Phys. Rev. Lett.* **128** 083604

[4] Caloz C, Alù A, Tretyakov S, Sounas D, Achouri K, and Deck-Léger Z L 2018 *Phys. Rev. Appl.* **10** 047001

[5] Scheucher M, Hilico A, Will E, Volz J, and Rauschenbeutel A 2016 *Science* **354** 1577

[6] Sliwa K M, Hatridge M, Narla A, Shankar S, Frunzio L, Schoelkopf R J, and Devoret M H 2015 *Phys. Rev. X* **5** 041020

[7] Linkhart D K 2014 *Microwave Circulator Design* (Artech House)

[8] Jalas D, Petrov A, Eich M, Freude W, Fan S H, Yu Z F, Baets R, Popović M, Melloni A, Joannopoulos J D *et al.* 2013 *Nat. Photonics* **7** 579

[9] Potton R J 2004 *Rep. Prog. Phys.* **67** 717

[10] Kamal A, Clarke J, and Devoret M H 2011 *Nat. Phys.* **7** 311

[11] Gauthier D J, Narum P, and Boyd R W 1986 *Opt. Lett.* **11** 623

[12] Ballato J and Snitzer E 1995 *Appl. Opt.* **34** 6848

[13] Snetkov I L, Voitovich A V, Palashov O V, and Khazanov E A 2014 *IEEE J. Quantum Electron.* **50** 434

[14] Starobor A, Mironov E, and Palashov O 2019 *Opt. Lett.* **44** 1297

[15] Kang M S, Butsch A, and Russell P S J 2011 *Nat. Photonics* **5** 549

[16] Huang D, Pintus P, Zhang C, Morton P, Shoji Y, Mizumoto T, and Bowers J E 2017 *Optica* **4** 23
[17] Cirac J I, Zoller P, Kimble H J, and Mabuchi H 1997 *Phys. Rev. Lett.* **78** 3221
[18] Reiserer A and Rempe G 2015 *Rev. Mod. Phys.* **87** 1379
[19] Lodahl P, Mahmoodian S, Stobbe S, Rauschenbeutel A, Schneeweiss P, Volz J, Pichler H, and Zoller P 2017 *Nature* **541** 473
[20] Zhang S, Hu Y, Lin G, Niu Y, Xia K, Gong J, and Gong S 2018 *Nat. Photonics* **12** 744
[21] Shen Z, Zhang Y L, Chen Y, Sun F W, Zou X B, Guo G C, Zou C L, and Dong C H 2018 *Nat. Commun.* **9** 1797
[22] Ren Y L, Ma S L, Xie J K, Li X K, Cao M T, and Li F L 2022 *Phys. Rev. A* **105** 013711
[23] Kimble H J 2008 *Nature* **453** 1023
[24] Alshowkan M, Williams B P, Evans P G, Rao N S V, Simmerman E M, Lu H H, Lingaraju N B, Weiner A M, Marvinney C E, Pai Y Y *et al.* 2021 *PRX Quantum* **2** 040304
[25] Ren Y L, Ma S L, Xie J K, and Li F L 2023 *Appl. Phys. Lett.* **122** 244002
[26] Zhang F, Ren J, Shan L, Duan X, Li Y, Zhang T, Gong Q, and Gu Y 2019 *Phys. Rev. A* **100** 053841
[27] Xia K, Lu G, Lin G, Cheng Y, Niu Y, Gong S, and Twamley J 2014 *Phys. Rev. A* **90** 043802
[28] Sayrin C, Junge C, Mitsch R, Albrecht B, O'Shea D, Schneeweiss P, Volz J, and Rauschenbeutel A 2015 *Phys. Rev. X* **5** 041036
[29] Tang L, Tang J S, Zhang W D, Lu G W, Zhang H, Zhang Y, Xia K Y, and Xiao M 2019 *Phys. Rev. A* **99** 043833
[30] Tang J S, Nie W, Tang L, Chen M, Su X, Lu Y, Nori F, and Xia K 2022 *Phys. Rev. Lett.* **128** 203602
[31] Yang P, Li M, Han X, He H, Li G, Zou C L, Zhang P, Qian Y, and Zhang T 2023 *Laser & Photonics Rev.* **17** 2200574
[32] Wang D W, Zhou H T, Guo M J, Zhang J X, Evers J, and Zhu S Y 2013 *Phys. Rev. Lett.* **110** 093901
[33] Horsley S A R, Wu J H, Artoni M, and La Rocca G C 2013 *Phys. Rev. Lett.* **110** 223602
[34] Sounas D L and Alù A 2017 *Nat. Photonics* **11** 774
[35] Cotrufo M, Cordaro A, Sounas D L, Polman A, and Alù A 2024 *Nat. Photonics* **18** 81
[36] Yang P F, Xia X W, He H, Li S K, Han X, Zhang P, Li G, Zhang P F, Xu J P, Yang Y P *et al.* 2019 *Phys. Rev. Lett.* **123** 233604
[37] Chang L, Jiang X, Hua S, Yang C, Wen J, Jiang L, Li G, Wang G, and Xiao M 2014 *Nat. Photonics* **8** 524
[38] Guo X, Zou C L, Jung H, and Tang H X 2016 *Phys. Rev. Lett.* **117** 123902
[39] Cao Q T, Wang H, Dong C H, Jing H, Liu R S, Chen X, Ge L, Gong Q, and Xiao Y F 2017 *Phys. Rev. Lett.* **118** 033901
[40] Sounas D L, Soric J, and Alù A 2018 *Nat. Electron.* **1** 113
[41] Tang L, Tang J S, Wu H D, Zhang J, Xiao M, and Xia K Y 2021 *Photonics Res.* **9** 1218
[42] Pan R K, Tang L, Xia K, and Nori F 2022 *Chin. Phys. Lett.* **39** 124201
[43] Xia K, Nori F, and Xiao M 2018 *Phys. Rev. Lett.* **121** 203602
[44] Li E Z, Ding D S, Yu Y C, Dong M X, Zeng L, Zhang W H, Ye Y H, Wu H Z, Zhu Z H, Gao W, Guo G C, and Shi B S 2020 *Phys. Rev. Res.* **2** 033517
[45] Liang C, Liu B, Xu A N, Wen X, Lu C, Xia K, Tey M K, Liu Y C, and You L 2020 *Phys. Rev. Lett.* **125** 123901
[46] Dong M X, Xia K Y, Zhang W H, Yu Y C, Ye Y H, Li E Z, Zeng L, Ding D S, Shi B S, Guo G C, and Nori F 2021 *Sci. Adv.* **7** eabe8924
[47] Tang L, Tang J S, and Xia K Y 2022 *Adv. Quantum Technol.* **5** 2200014
[48] Hafezi M and Rabl P 2012 *Opt. Express* **20** 7672
[49] Kim J, Kuzyk M C, Han K, Wang H, and Bahl G 2015 *Nat. Phys.* **11** 275
[50] Shen Z, Zhang Y L, Chen Y, Zou C L, Xiao Y F, Zou X B, Sun F W, Guo G C, and Dong C H 2016 *Nat. Photonics* **10** 657
[51] Fang K, Luo J, Metelmann A, Matheny M H, Marquardt F, Clerk A A, and Painter O 2017 *Nat. Phys.* **13** 465
[52] Kittlaus E A, Jones W M, Rakich P T, Otterstrom N T, Muller R E, and Rais-Zadeh M 2021 *Nat. Photonics* **15** 43
[53] Huang R, Miranowicz A, Liao J Q, Nori F, and Jing H 2018 *Phys. Rev. Lett.* **121** 153601
[54] Chai C Z, Zhao H Q, Tang H X, Guo G C, Zou C L, and Dong C H 2020 *Laser & Photonics Rev.* **14** 1900252
[55] Fan B, Nasir M E, Nicholls L H, Zayats A V, and Podolskiy V A 2019 *Adv. Opt. Mater.* **7** 1801420
[56] Carothers K J, Norwood R A, and Pyun J 2022 *Chem. Mater.* **34** 2531
[57] Toyoda S, Abe N, and Arima T 2019 *Phys. Rev. Lett.* **123** 077401
[58] Ren Y L, Ma S L, Xie J K, Li X K, and Li F L 2021 *Opt. Express* **29** 41399
[59] Bi L, Hu J, Jiang P, Kim D H, Dionne G F, Kimerling L C, and Ross C A 2011 *Nat. Photonics* **5** 758
[60] Duggan R, del Pino J, Verhagen E, and Alù A 2019 *Phys. Rev. Lett.* **123** 023602
[61] Yan W, Yang Y, Liu S, Zhang Y, Xia S, Kang T, Yang W, Qin J, Deng L, and Bi L 2020 *Optica* **7** 1555
[62] Lin Z, Ramezani H, Eichelkraut T, Kottos T, Cao H, and Christodoulides D N 2011 *Phys. Rev. Lett.* **106** 213901
[63] Wang Y P, Rao J W, Yang Y, Xu P C, Gui Y S, Yao B M, You J Q, and Hu C M 2019 *Phys. Rev. Lett.* **123** 127202
[64] Wu J H, Artoni M, and La Rocca G C 2014 *Phys. Rev. Lett.* **113** 123004
[65] Feng L, Xu Y L, Fegadolli W S, Lu M H, Oliveira J E B, Almeida V R, Chen Y F, and Scherer A 2013 *Nat. Mater.* **12** 108
[66] Inoue T, Noguchi N, Yoshida M, Kim H, Asano T, and Noda S 2023 *Phys. Rev. Appl.* **20** L011001
[67] Walls D F and Milburn G J 2007 *Quantum Optics* (Berlin: Springer)
[68] Ling H Y 1994 *J. Opt. Soc. Am. A* **11** 754
[69] Dong L, Jiang H, Chen H, and Shi Y 2010 *J. Appl. Phys.* **107** 093101
[70] Rosenberg R, Rubinstein C B, and Herriott D R 1964 *Appl. Opt.* **3** 1079
[71] Li Y Q, Steuerman D W, Berezovsky J, Seferos D S, Bazan G C, and Awschalom D D 2006 *Appl. Phys. Lett.* **88** 193126
[72] Hu X X, Wang Z B, Zhang P *et al.* 2021 *Nat. Commun.* **12** 2389
[73] Lipson S G, Lipson H, and Tannhauser D S 2010 *Optical Physics* (Cambridge: Cambridge University Press)
[74] Collett M J and Gardiner C W 1984 *Phys. Rev. A* **30** 1386
[75] Gardiner C W and Collett M J 1985 *Phys. Rev. A* **31** 3761
[76] Combes J, Kerckhoff J, and Sarovar M 2017 *Adv. Phys.: X* **2** 784
[77] Ao Y, Hu X, You Y, Lu C, Fu Y, Wang X, and Gong Q 2020 *Phys. Rev. Lett.* **125** 013902
[78] Mikhaylovskiy R V, Hendry E, and Kruglyak V V 2012 *Phys. Rev. B* **86** 100405
[79] Zak J, Moog E R, Liu C, and Bader S D 1991 *Phys. Rev. B* **43** 6423
[80] Shiraishi K, Tajima F, and Kawakami S 1986 *Opt. Lett.* **11** 82
[81] Shalaby M, Peccianti M, Ozturk Y, and Morandotti R 2013 *Nat. Commun.* **4** 1558
[82] Mironov E A, Voitovich A V, and Palashov O V 2019 *Laser Phys. Lett.* **17** 015001
[83] Slezák O, Vojna D, Pilař J, Divoký M, Denk O, Hanuš M, Navrátil P, Smrž M, Lucianetti A, and Mocek T 2023 *Opt. Lett.* **48** 3471
[84] Vojna D, Slezák O, Lucianetti A, and Mocek T 2019 *Appl. Sci.* **9** 3160
[85] Ikesue A and Aung Y L 2018 *J. Am. Ceram. Soc.* **101** 5120

Supplemental Material: Reversible optical isolators and quasi-circulators using a magneto-optical Fabry–Pérot cavity

Tiantian Zhang(张天天)[1], Wenpeng Zhou(周文鹏)[1], Zhixiang Li(李志向)[1], Yutao Tang(唐宇涛)[2],
Fan Xu(许帆)[2], Haodong Wu(吴浩东)[1], Han Zhang(张涵)[3], Jiang-Shan Tang(唐江山)[1*],
Ya-Ping Ruan(阮亚平)[1*], and Keyu Xia(夏可宇)[1,4*]

[1] *College of Engineering and Applied Sciences, National Laboratory of Solid State Microstructures, and Collaborative Innovation Center of Advanced Microstructures, Nanjing University, Nanjing 210093, China*
[2] *Shenzhen Shaanxi Coal Hi-tech Research Institute Co., Ltd, Shenzhen 518083, China*
[3] *School of Physics, Nanjing University, Nanjing 210023, China*
[4] *Jiangsu Key Laboratory of Artificial Functional Materials, Nanjing University, Nanjing 210023, China*

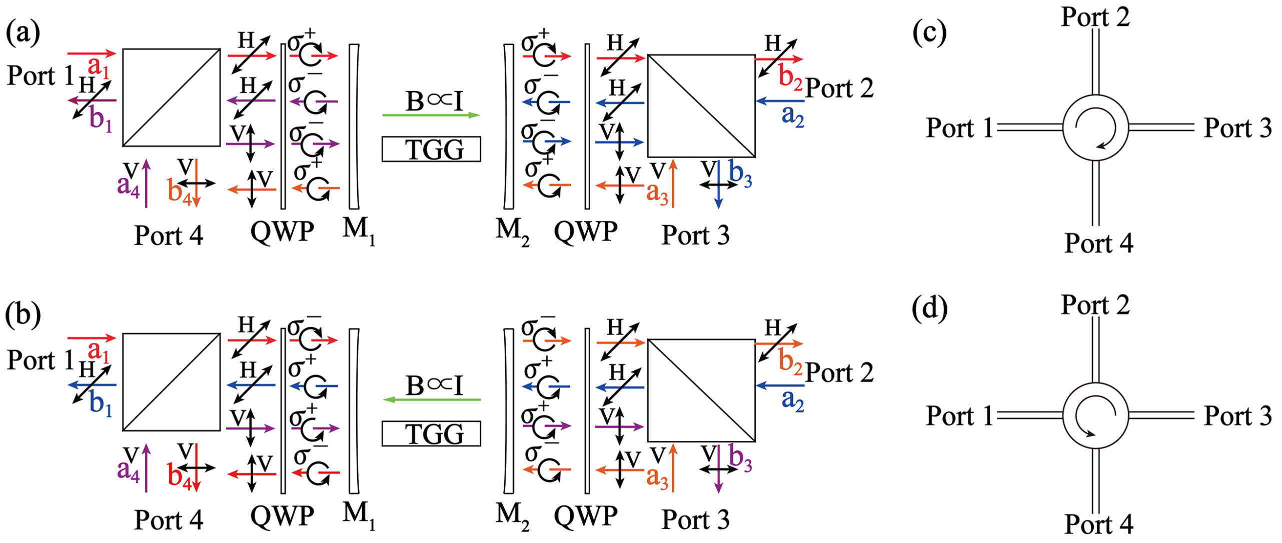

Fig. S1. [(a), (b)] Conceptual schematics of the reversible optical isolators and 4-port circulators. Here, we use arrows of different colors to represent the light incident from different ports.Experimental diagrams of the clockwise (CW) (a) and counterclockwise (CCW) (b) configurations comprise a magneto-optical Fabry–Pérot (MOFP) cavity, a pair of quarter wave plates (QWPs), and a pair of polarization beam splitters (PBSs), respectively. The magnetic direction of the CCW configuration is opposite to that of the CW configuration. The combination of PBSs and QWPs locks the $\sigma^{\pm}$ polarization and the optical propagation direction in the MOFP cavity. Black arrows indicate local optical polarization. Here, σ^{+} and σ^{-} polarizations are defined by the rotating direction of the electric-field vectors relative to the direction of the magnetic field. The circulation of the polarized light is achieved through PBSs. TGG: terbium gallium garnet. [(c), (d)] Schematic CW (c) and CCW (d) 4-port circulators depicting the flowing direction of light in the CW and CCW configurations, respectively.

A. The 4-port CW circulator

The optical transmission matrix of the four-port CW circulator can be written as:

$$\begin{pmatrix} b_1 \\ b_2 \\ b_3 \\ b_4 \end{pmatrix} = \begin{pmatrix} 0 & T_- & 0 & R_- \\ T_+ & 0 & R_+ & 0 \\ 0 & R_- & 0 & T_- \\ R_+ & 0 & T_+ & 0 \end{pmatrix} \begin{pmatrix} a_1 \\ a_2 \\ a_3 \\ a_4 \end{pmatrix}, \tag{S1}$$

when $\delta_+ = 0$, the transfer matrix can be written as:

$$\begin{pmatrix} b_1 \\ b_2 \\ b_3 \\ b_4 \end{pmatrix} = \begin{pmatrix} 0 & 0 & 0 & 1 \\ 1 & 0 & 0 & 0 \\ 0 & 1 & 0 & 0 \\ 0 & 0 & 1 & 0 \end{pmatrix} \begin{pmatrix} a_1 \\ a_2 \\ a_3 \\ a_4 \end{pmatrix}, \tag{S2}$$

---

[*] Electronic address: js.tang@nju.edu.cn; ruanyaping@nju.edu.cn; keyu.xia@nju.edu.cn

which is the scattering matrix of an ideal circulator, proving that our system can be used as a four-port optical circulator. The optical path implements a 4-port clockwise (CW) circulator, along port 1 → 2 → 3 → 4 → 1, as shown in Figs. S1(a) and S1(c).

B. The 4-port CCW circulator

When the optical path is reversed, the magnetic field can be reversed to ensure smooth light transmission. The optical transmission matrix of the CCW circulator can be expressed as:

$$\begin{pmatrix} b_1 \\ b_2 \\ b_3 \\ b_4 \end{pmatrix} = \begin{pmatrix} 0 & T_+ & 0 & R_+ \\ T_- & 0 & R_- & 0 \\ 0 & R_+ & 0 & T_+ \\ R_- & 0 & T_- & 0 \end{pmatrix} \begin{pmatrix} a_1 \\ a_2 \\ a_3 \\ a_4 \end{pmatrix}, \tag{S3}$$

when $\delta_+ = 0$, the transfer matrix can be written as:

$$\begin{pmatrix} b_1 \\ b_2 \\ b_3 \\ b_4 \end{pmatrix} = \begin{pmatrix} 0 & 1 & 0 & 0 \\ 0 & 0 & 1 & 0 \\ 0 & 0 & 0 & 1 \\ 1 & 0 & 0 & 0 \end{pmatrix} \begin{pmatrix} a_1 \\ a_2 \\ a_3 \\ a_4 \end{pmatrix}, \tag{S4}$$

which is also the scattering matrix of an ideal circulator, proving that our system can still function as a four-port optical circulator when optical path reverses. The light path exhibits a counterclockwise (CCW) circulation of photons (port 4 → 3 → 2 → 1 → 4), see Figs. S1(b) and S1(d).

C. Experimental setup

As shown in Fig. S2, the system, comprising mirrors, beam splitters (BSs), and polarization beam splitters (PBSs), is designed for investigating the functionality of 4-port optical circulators. In this setup, we achieve the division of the original two incident beams into four by employing a combination of two sets of BSs and one set of reflectors. Subsequently, these four beams are individually coupled into the MOCFP cavity through four distinct ports.

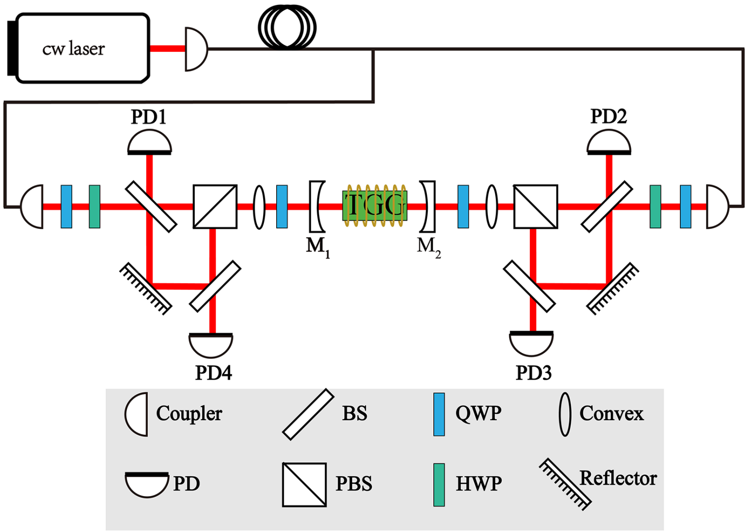

Fig. S2. Schematic experimental setup for the 4-port circulators based on the MOFP cavity. PD: photon detector; BS: beam splitter; PBS: polarization beam splitter; M: mirror; QWP: quarter-wave plate; HWP: half-wave plate; Convex: convex lens; Reflector: total internal reflection mirror.